ROYAL SOCIETY
OF CHEMISTRY

PAPER

Check for updates

An ultrathin Al₂O₃ bridging layer between CdS and ZnO boosts photocatalytic hydrogen production†

Dandan Ma,[a] Zhenyu Wang,[a] Jian-Wen Shi, [ID] *[a] Yajun Zou,[a] Yixuan Lv,[a] Xin Ji,[a] Zhihui Li,[a] Yonghong Cheng[a] and Lianzhou Wang [ID] *[b]

The rapid separation and transfer of photogenerated charge carriers are the essential criteria for high photocatalytic efficiency. Heterostructures (HSs) composed of several semiconductors can take advantage of energy level difference to promote the separation and transfer of photogenerated electrons and holes, where the interface between semiconductors is the most critical position which directly determines the transfer mechanism of photogenerated charge carriers, and ultimately determines the photocatalytic efficiency. Herein, an ultrathin Al₂O₃ bridging layer is intentionally introduced into the interface between CdS and ZnO by using an atomic layer deposition (ALD) method, and the resultant CdS@Al₂O₃@ZnO catalyst exhibits a significantly enhanced H₂ evolution rate (1190 μmol h⁻¹ m⁻²) and a high apparent quantum efficiency (AQE, 31.14% at a wavelength of 420 nm). It is revealed that the ultrathin Al₂O₃ bridging layer converts the original Z-scheme mechanism of photogenerated charge carriers in the CdS@ZnO catalyst into a modified type II mechanism in the CdS@Al₂O₃@ZnO catalyst, where the photogenerated electrons are tunnelled from the CdS core to the ZnO shell and then are depleted by H₂O effectively in time to produce H₂. Meanwhile, the photogenerated holes are consumed efficiently by the fixed negative charges of Al₂O₃. Detailed characterization reveals that the lattice mismatch between wurtzite ZnO and wurtzite CdS is effectively passivated by the Al₂O₃ interlayer, facilitating the uniform deposition of the ZnO layer, which promotes the close contact between interfaces, suppressing the recombination of charge carriers. This work provides a new strategy for controlling the dominant transfer mechanisms of photogenerated electrons and holes in HSs through interface regulation.

1. Introduction

Heterostructures (HSs) consisting of several semiconductors have the combined merits of different semiconductors that complement each other, which is important to overcome the inherent shortcomings of single semiconductors, such as the limited light absorption and the restricted separation efficiency of photogenerated electrons and holes.[1–4] Therefore, HSs have been considered as a promising strategy to construct new photocatalysts with high activity for hydrogen production from the water splitting process.[5–7] To date, studies on HSs composed of binary (CdS/ZnS, TiO₂@gC₃N₄),[7,8] ternary (graphene–CdS–MoS₂, In₂O₃/InCd₂S₄/In₂S₃, ZnS/CdS/ZnO)[9–11] and quaternary components (ZnO/ZnS/CdS/CuInS₂, TiO₂/CdS/Co–Pi)[12,13] have

been widely carried out, and all HSs exhibit higher activity than single semiconductors because photogenerated electrons and holes in HSs can migrate to different semiconductors, efficiently suppressing the recombination.[14–18] It has been widely demonstrated that the transfer of photogenerated electrons and holes in HSs follows several mechanisms, such as type I (nested energy band distribution),[19,20] type II (staggered band distribution),[21,22] Z-scheme,[23,24] *etc.* For a HS, the transfer mechanisms of photogenerated electrons and holes in it are not constant, but vary with the environment of the HS, especially the surface and interface of the HS. In our previous work, we introduced Au nanoparticles (NPs) into the interface of C-doped TiO₂ and g-C₃N₄, and found that the transfer mechanism of charge carriers changed from type II into Z-scheme.[23,25] Recently, we successfully prepared an Au decorated hollow ZnO@ZnS HS, where two kinds of Au NPs located on the surface and at the interface of ZnO@ZnS were disclosed, which played different roles and resulted in different transfer mechanisms of charge carriers, respectively.[26] Therefore, we believe that the dominant transfer mechanisms of photogenerated electrons and holes in HSs can be effectively adjusted and controlled according to the ultimate goal.

[a]State Key Laboratory of Electrical Insulation and Power Equipment, Center of Nanomaterials for Renewable Energy, School of Electrical Engineering, Xi'an Jiaotong University, Xi'an 710049, China. E-mail: jianwen.shi@mail.xjtu.edu.cn

[b]Nanomaterials Centre, School of Chemical Engineering, Australian Institute for Bioengineering and Nanotechnology, The University of Queensland, St. Lucia, Brisbane, QLD 4072, Australia. E-mail: l.wang@uq.edu.au

† Electronic supplementary information (ESI) available. See DOI: 10.1039/d0ta03933k

In an early study,[27] we successfully constructed a CdS@ZnO HS with a core@shell structure by using an atomic layer deposition (ALD) method. The H_2 evolution rate of the obtained CdS@ZnO was 4.1 times higher than the highest reported value $(17.40 \text{ mmol g}^{-1} \text{ h}^{-1})$[28] at that time among the CdS–ZnO catalyst systems, and a direct Z-scheme mechanism was confirmed to dominate the transfer of photogenerated charge carriers. However, there is still much room for improving its photocatalytic H_2 evolution when the optimization of the HS is taken into consideration: (1) owing to the Z-scheme mechanism, the photogenerated electrons are accumulated on the conduction band of the CdS core, which cannot be consumed effectively in time by H_2O to produce H_2 due to the barrier of the ZnO shell; (2) the ZnO shell is adhered to the CdS core as nanoparticles rather than a layer due to the lattice mismatch between wurtzite ZnO and wurtzite CdS, which is not conducive to the formation of a close contacted high quality interface between the two semiconductors, resulting in inefficient transfer of photogenerated charge carriers. If the photogenerated electrons can be transferred from the CdS core to the ZnO shell, and the lattice mismatch between wurtzite ZnO and wurtzite CdS can be overcome, the resultant CdS@ZnO HS is expected to exhibit significantly enhanced photocatalytic H_2 evolution.

Based on the above considerations, in this work, we selectively introduced an ultrathin Al_2O_3 interlayer between CdS and ZnO by using the ALD method. It is found that the introduction of the Al_2O_3 interlayer is efficient in addressing the two above-mentioned problems simultaneously. In the resultant CdS@Al_2O_3@ZnO HS, the photogenerated electrons were transferred from the CdS core to the ZnO shell due to a tunneling effect induced by the Al_2O_3 interlayer, and meanwhile the photogenerated holes were consumed efficiently by the negative fixed charges of the Al_2O_3 interlayer, resulting in a modified type II transfer mechanism. Furthermore, the lattice mismatch between wurtzite ZnO and wurtzite CdS was effectively passivated by the Al_2O_3 interlayer, facilitating the uniform deposition of the ZnO layer, which promoted the close contact between interfaces, effectively suppressing the recombination of charge carriers. The photocatalytic performance of the CdS@Al_2O_3@ZnO for H_2 evolution was further improved, benefiting from the dual roles of the Al_2O_3 interlayer.

2. Experimental section

2.1 Synthesis of CdS nanoparticles

CdS nanoparticles (NPs) were fabricated by using a hydrothermal method according to our previous report.[27] To be specific, 100 mL of sodium sulfide (Na_2S, 0.14 M) solution was slowly added to 125 mL of cadmium acetate dihydrate ($Cd(CH_3COO)_2 \cdot 2H_2O$, 0.14 M) solution and stirred for 24 h. The obtained mixture was stewed for another 24 h, and then washed with deionized water three times. After that, the yellow pulp was dispersed in 80 mL of deionized water, sealed into a 100 mL stainless steel Teflon-lined autoclave and heated at 200 °C for 72 h. After cooling down to room temperature, the obtained product was washed with deionized water and ethanol three times and dried at 80 °C, resulting in CdS NPs.

2.2 Atomic layer deposition of Al_2O_3 and ZnO

The CdS@Al_2O_3@ZnO multi-shell heterostructure was prepared by using a consecutive atomic layer deposition method. The substrate sample was obtained by dripping 40 mg of CdS NPs (dispersed in ethanol) on an 8 inch silicon wafer which was then dried up at 60 °C. The substrate sample was then placed in a vacuum ALD reaction chamber (ALD 004, SENTECH, Germany). Trimethylaluminum (TMA) and diethyl zinc ($Zn(C_2H_5)_2$) were utilized as Al and Zn precursors for the deposition of Al_2O_3 and ZnO, respectively, and water was used as another precursor to provide the O source. Nitrogen served as a carrier gas. The temperature of the reaction chamber was set at 250 °C to ensure the evaporation of precursors during the reaction, and the deposition amount of the shell layer was controlled by the number of deposition cycles. One standard deposition cycle consisted of four steps: injection of the Zn or Al precursor, nitrogen flow, injection of the oxygen precursor, and nitrogen flow. The number of deposition cycles for Al_2O_3 was 1, 2, 6 and 10, while the number of deposition cycles for ZnO was 100. The obtained CdS@Al_2O_3@ZnO core–shell structures were denoted as Cd@Al_x@Zn, where x is the number of deposition cycles of Al_2O_3.

In addition, a control sample, CdS@ZnO@Al_2O_3 (Cd@Zn@Al), was fabricated by switching the deposition order of Al_2O_3 and ZnO. The number of deposition cycles of ZnO and Al_2O_3 was 100 and 2, respectively, and the obtained sample was denoted as Cd@Zn@Al_2.

In order to get pure Al_2O_3 and minimize the influence of the synthesis method on the properties of the product, we employed the same ALD method in the fabrication of Al_2O_3 by using an 8 inch silicon plate as the substrate. 200 deposition cycles were applied to get enough amount of Al_2O_3 for the test. After deposition, the white sample was collected by scraping carefully with a clean blade.

2.3 Photocatalytic hydrogen generation

The photocatalytic water splitting reaction was carried out in a top-irradiation quartz cell connected to a closed glass gas circulation system (CEL-SPH2N, Beijing), and a 300 W xenon arc lamp was used as the simulated solar light source. 10 mg of the as-synthesized photocatalyst was dispersed in 25 mL of deionized water containing 0.35 M sodium sulfide and 0.25 M sodium sulfite anhydrous, and 1 wt% Pt was added as the co-catalyst. The amount of H_2 evolved under irradiation was monitored *via* a TCD gas chromatograph (GC-9720). Magnetic stirring was used during the water splitting experiment to ensure homogeneity of the suspension.

Besides the mass of catalysts, the light absorption ability and specific surface area are two of the most crucial factors in the photocatalytic reaction. Here, the multi-factor-normalized H_2 evolution rate was adopted to evaluate the photocatalytic performance of the catalysts.[29,30] CdS was used as the reference sample in the normalization treatment; for instance, the light absorption ability of CdS is defined as 1, and the light absorption ability of one catalyst *versus* CdS, named relative light absorption coefficient ($r_{Abs.}$), is determined from the ratio of

11032 | *J. Mater. Chem. A*, 2020, **8**, 11031–11042

This journal is © The Royal Society of Chemistry 2020

total absorption intensity of the studied catalyst and that of CdS. The multi-factor-normalized H_2 evolution rate was determined from the following equation:

$$R(H_2) = \frac{N(H_2)}{t \times S_{BET} \times r_{Abs.}}$$

where, $R(H_2)$ is the relative H_2 evolution rate and $N(H_2)$ is the amount of hydrogen generated from the water splitting reaction during a certain period of time. t, S_{BET} and $r_{Abs.}$ are the reaction time, specific surface area and relative light absorption coefficient of the catalysts, respectively.

In the long-term stability test, every cycle was maintained for 5 hours. After a cycle, the pressure of the gas circulation system was balanced by connecting directly to environmental conditions, while the TCD gas chromatograph detection system was pumped with N_2 to remove the residual H_2. At the same time, the sacrificial agent with Na_2SO_3 and Na_2S was refreshed for the next cycle. All the reaction conditions in the long-term stability test were the same as for the above-mentioned photocatalytic H_2 evolution.

2.4 Characterization

X-ray diffraction (XRD) patterns were recorded on a Bruker AXS D2 Phaser instrument using CuK_{α} radiation in step mode between 20° and 60°. Transmission electron microscopy (TEM) and energy dispersive spectroscopy (EDS) mapping images were obtained on a JEOL JEM-2100F microscope operating at a voltage of 200 kV. Scanning electron microscopy (SEM) images were obtained on a field emission scanning electron microscope (Gemini SEM 500). X-ray photoelectron spectroscopy (XPS) analyses were performed on a Thermo Fisher ESCALAB Xi+ analyzer with aluminum K_{α} radiation. UV-vis absorption spectra were recorded with a UV-Vis-NIR spectrometer (JASCO, V-670). Photoluminescence (PL) spectra and fluorescence lifetimes were measured using a fluorescence spectrometer (Edinburgh Instruments FLS 980), and the excitation wavelength was 370 nm. Transient photocurrent response measurement and electrochemical impedance spectroscopy (EIS) were carried out in a standard three-compartment cell, where a saturated calomel electrode (SCE) was used as the reference electrode. To avoid the effect of dissolved Pt^{2+} on the measurement,[31,32] carbon paper (1 cm × 1 cm) was utilized as the counter electrode, and the working electrode was made by loading the catalyst on fluorine-doped tin oxide (FTO, 7 Ω per square) glasses. 0.1 mol L^{-1} Na_2SO_4 solution was used as the electrolyte, and a 300 W Xe lamp was utilized as the light source. Light on and off operation was controlled by a shutter every 20 seconds and the response of transient photocurrent was recorded on a CHI 660 E electrochemical workstation (Shanghai, China).

2.5 Detection of hydroxyl radicals

Hydroxyl radicals ($\cdot$OH) were detected by the PL method using terephthalic acid (TA) as a probe molecule. In a typical procedure, 10 mg of the sample was dispersed in a 20 mL aqueous solution of 5×10^{-4} M TA and 2×10^{-3} M NaOH. The suspension was irradiated under a 300 W Xe lamp for 10 min with stirring, after which, a solution was obtained thorough centrifugation to remove catalyst particles. Subsequently, the solution was analyzed under the excitation of 315 nm wavelength by using a FLS980 fluorescence spectrometer.

2.6 Computational details

All calculations were performed using periodic density functional theory (DFT) through the Vienna Ab Initio Simulation Package (VASP).[33–35] The interaction between the core and valence electrons was described using the projector-augmented wave (PAW) method.[36,37] The PBE sol functional was applied for geometry optimization.[38] However, the hybrid Heyd–Scuseria–Ernzerhof functional (HSE06) including 25% screened Hartree–Fock (HF) exchange,[9,40] hybrid PBE0 functional using 25% HF exchange,[41,42] and HSE with 37.5% HF exchange (HSE375) were employed for the electronic property calculations of wurtzite CdS, γ-Al_2O_3 and wurtzite ZnO, respectively, because these parameters were found to reproduce their band gaps.[43–45] A plane wave cutoff energy of 560 eV was applied for all electronic calculations, with Γ-centred k-point meshes of 6 × 6 × 4, 8 × 8 × 4 and 8 × 8 × 4 for unit cells of CdS, Al_2O_3 and ZnO, respectively, and was determined to be sufficient to converge the total energy of each system to within 10^{-5} eV per atom.

Three two-phase heterojunctions were built using 1 × 2 CdS (110)/1 × 1 Al_2O_3 (−111), 1 × 1 Al_2O_3 (−111)/2 × 2$\sqrt{3}$ ZnO (001) and 1 × 1 CdS (110)/2 × $\sqrt{3}$ ZnO (001). These combinations were necessary to balance the total number of atoms and the strain caused by the mismatch of two phases. The electrostatic potentials of the heterojunctions were calculated using the hybrid HSE06 including 25% screened Hartree–Fock exchange.[39,40] A 20 Å vacuum was employed for all surface slabs to vanish wave function overlaps across the vacuum region. The ionization potential was calculated using the core-level alignment approach of Wei and Zunger,[46] and the non-polar CdS (110), Al_2O_3 (−111) and ZnO (100) surfaces were chosen.

3. Results and discussion

3.1 The microstructure and photocatalytic performance of Cd@Al_2@Zn

Fig. 1a shows the XRD patterns of the four selected samples, CdS, Cd@Zn, Cd@Al_2 and Cd@Al_2@Zn. It can be observed that all samples display the dominant characteristic peaks of wurtzite CdS (JCPDS 41-1049).[47–49] After 100 deposition cycles of ZnO, several weak peaks at 30–35° can be found from the XRD of Cd@Zn, and their low intensity can be attributed to the very small amount as well as the high dispersity of ZnO.[48–51] No XRD signal of Al_2O_3 was detected, which is mainly due to the amorphous nature and very small amount of Al_2O_3.[16,43] The XRD spectra of the Si substrate before and after Al_2O_3 deposition are presented in Fig. S1.† The wide diffraction peaks between 15 and 35 degrees come from the SiO_2 on the surface of the Si substrate, and no new peak appeared even after 200 cycles of Al_2O_3 deposition, indicating the amorphous nature of Al_2O_3.[43,52,53] It should be noticed that with the same number of

This journal is © The Royal Society of Chemistry 2020
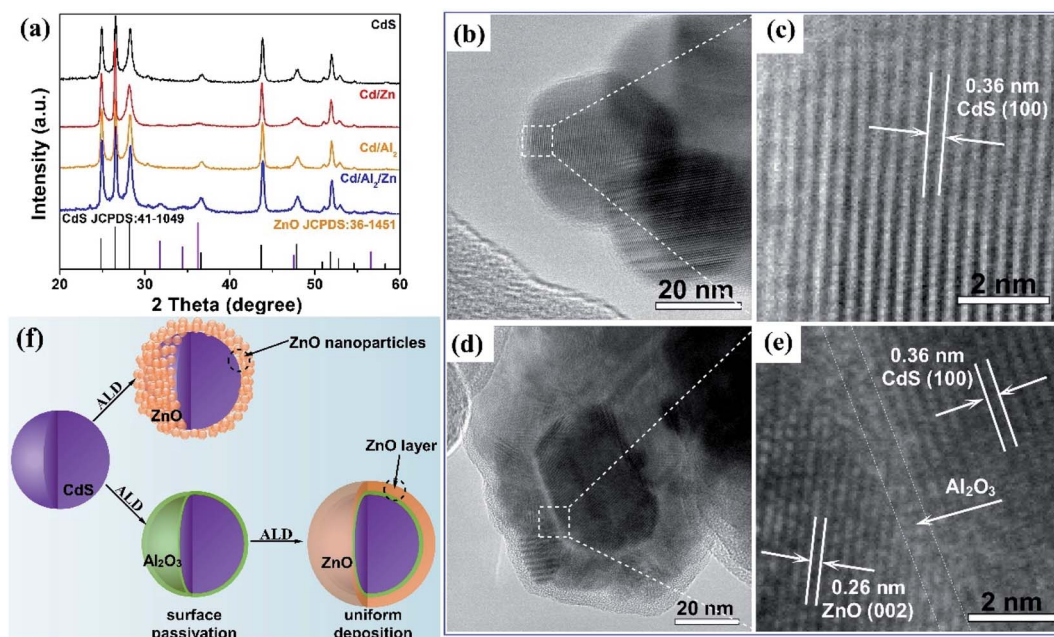
J. Mater. Chem. A, 2020, **8**, 11031–11042 | **11033**

Fig. 1 (a) XRD spectra of CdS, Cd@Zn, Cd@Al₂ and Cd@Al₂@Zn (the peaks of CdS and ZnO are marked by black and purple graphic patterns, respectively). (b and d) TEM and (c and e) HRTEM images of (b and c) CdS and (d and e) Cd@Al₁₀@Zn. (f) Schematic view of the interface difference between Cd@Zn and Cd@Al@Zn fabricated by the ALD method.

deposition cycles of the ZnO layer, the ZnO peaks in the XRD pattern of Cd@Al₂@Zn were obviously stronger than those of Cd@Zn, and thus we suppose that the introduction of Al₂O₃ facilitates the deposition of the ZnO layer.

The above assumption can be confirmed by TEM characterization. The pristine CdS presented a uniform spherical morphology with an average diameter of 35 ± 5 nm and a smooth surface (Fig. 1b). The characteristic (100) lattice fringes (0.36 nm) of wurtzite CdS can be clearly observed from Fig. 1c, indicating the good crystallinity of CdS NPs.[48] The TEM images of Cd@Zn show the deposited ZnO as nanoparticles attached on the surface of CdS (Fig. S2a†). The distinguished lattice spacing of about 0.26 nm (Fig. S2b†) matched well with the (002) interplanar spacing of wurtzite ZnO (JCPDS 36-1451).[54–56] For easy observation, the TEM of Cd@Al₁₀@Zn was carried out. As shown in Fig. 1d and e, the surface of CdS was covered by the Al₂O₃ layer and ZnO layer, and a light-colored Al₂O₃ layer appeared between the CdS core and the ZnO shell (Fig. 1d). The relative position of CdS, Al₂O₃ and ZnO can be further identified by EDX mapping. As shown in Fig. S3,† Cd and S signals are located at the center of the particles while the outer position is dominated by O, Zn and Al elements. In addition, the overlap images of S&Cd&Zn and Cd&Al&Zn are in accord with the HADDF image of the sample, demonstrating the formation of the core–shell heterostructure. Two kinds of lattice parameters, corresponding to CdS (0.36 nm) and ZnO (0.26 nm), can be observed from the HRTEM image (Fig. 1e), and the light-colored region (labeled with a white dotted line in Fig. 1e) shows the amorphous characteristics of the Al₂O₃ layer with an average thickness of about 1 nm. It should be noted that the ZnO deposited directly on the CdS core is in the form of

nanoparticles rather than a layer, which has been confirmed in our previous work.[48] The reason can be ascribed to the mismatched lattice between wurtzite ZnO and wurtzite CdS. After the wurtzite CdS core is wrapped by an amorphous Al₂O₃ layer, the wurtzite ZnO deposited on Cd@Al is a layer rather than nanoparticles, suggesting that the mismatched lattice between wurtzite ZnO and wurtzite CdS is passivated by the amorphous Al₂O₃ layer. As illustrated in Fig. 1f, when Al₂O₃ is deposited on the surface of CdS, a uniform deposition layer and an intimate interface can be obtained due to the good surface compatibility of Al₂O₃. After that, diethyl zinc and water are alternatively pumped into the reaction chamber for the deposition of ZnO. The uniformly deposited Al₂O₃ provides an ideal substrate for the nucleation and growth of ZnO, thus playing the role of a seed layer. In addition, in the formation of the heterostructure, the good surface compatibility of Al₂O₃ helps shrink the mismatch and lattice distortion between CdS and ZnO and facilitates the formation of an intimately contacted interface, thus playing the role of a buffer layer. The SEM images (Fig. S4†) further verified the role of the Al₂O₃ interlayer in the deposition of the ZnO shell. A fluffy surface of the sample can be clearly observed from the SEM images of Cd@Zn (Fig. S4a and b†), which mainly comes from the uneven deposition of ZnO NPs. However, a relatively smooth surface was observed over the Cd@Al₁₀ and Cd@Al₁₀@Zn samples (Fig. S4c–f†). Since the same deposition procedure of ZnO was utilized in all samples, the different morphologies of ZnO in Cd@Zn and Cd@Al₁₀@Zn can be ascribed to the Al₂O₃ interlayer.

UV-vis absorption spectroscopy and BET measurements were carried out to investigate the effect of the Al₂O₃ interlayer on the light absorption ability and specific surface area of the catalysts.

11034 | J. Mater. Chem. A, 2020, **8**, 11031–11042

This journal is © The Royal Society of Chemistry 2020

As shown in Fig. S5a,† no obvious change of light absorption ability was observed for the samples, this is because of the translucent properties of ZnO and Al_2O_3 as well as the very low loading amount of Al_2O_3. The deposition of ZnO and Al_2O_3 resulted in obvious change in the specific surface area of the samples, and as can be observed from Fig. S5c,† Cd@Zn displayed a much higher surface area than pure CdS due to the uneven deposition of ZnO, which can be confirmed by the results of SEM and TEM observation. After the introduction of the Al_2O_3 interlayer, the specific surface area of Cd@Al$_x$@Zn gradually decreased to a stable level, the same as that of CdS. Based on previous experiments and discussion, the decrease of surface area can be attributed to the introduction of a highly-surface-compatible-Al_2O_3 layer, which facilitated the uniform and dense deposition of the ZnO layer.

The photocatalytic performances of the samples were investigated by monitoring the hydrogen evolution rate. Chloroplatinic acid was added as the precursor to provide a Pt cocatalyst, and we detected the components of the solution by using ICP-MS and found there were no Pt ions in the solution after reaction, indicating that Pt ions have been reduced into Pt nanoparticles and deposited on the surface of the photocatalyst. Multi-factor-normalized H_2 evolution rate was adopted to give a more accurate determination of the photocatalytic activity of the samples, and the effect of light absorption ability was eliminated by the introduction of the relative light absorption coefficient ($r_{Abs.}$). As shown in Fig. 2a, CdS displayed a relatively low H_2 evolution rate of 45 μmol h^{-1} m^{-2} due to the serious charge recombination.[55,56] After depositing Al_2O_3, a slightly increased hydrogen generation ability was observed over the

Cd@Al$_x$ samples, which is much lower than that over Cd@Zn samples (548 μmol h^{-1} m^{-2}) due to the as-reported Z-scheme transfer mechanism between ZnO and CdS.[48,57,58] After a ZnO layer was deposited on the Cd@Al$_2$ sample, the photocatalytic activity of Cd@Al$_2$@Zn was significantly enhanced. As observed in Fig. 2b, the H_2 evolution rate climbed from 807 μmol h^{-1} m^{-2} for Cd@Al$_1$@Zn to 1190 μmol h^{-1} m^{-2} for Cd@Al$_2$@Zn, and then reduced to 1084 μmol h^{-1} m^{-2} for Cd@Al$_6$@Zn, suggesting that the Al_2O_3 interlayer with a suitable thickness contributes to the improvement of photocatalytic H_2 evolution performance of Cd@Al@Zn. As an important control sample, we fabricated Cd@Zn@Al$_2$ by switching the deposition order of ZnO and Al_2O_3, and the H_2 evolution ability of Cd@Zn@Al$_2$ (692 μmol h^{-1} m^{-2}) was much lower than that of Cd@Al$_2$@Zn (1190 μmol h^{-1} m^{-2}) (the H_2 evolution rates before normalization are shown in Fig. S6†). We carefully studied the hydrogen evolution rates of different CdS–ZnO based H_2 evolution improvement strategies reported in the literature (Table S2†), and found that the hydrogen evolution rate of 101.3 mmol h^{-1} g^{-1} (1190 μmol h^{-1} m^{-2}) over Cd@Al$_2$@Zn is the highest level. The result demonstrates that the introduction of the Al_2O_3 passivation interlayer is promising for improving the photocatalytic H_2 evolution ability. The apparent quantum efficiency (AQE) of Cd@Al$_2$@Zn at different wavelengths was further tested. As shown in Fig. 2c, the highest AQE value of about 31.14% was obtained at a wavelength of 420 nm. A long-term cycle test exhibited that no obvious difference in photocatalytic ability (Fig. 2d) and crystal structure (Fig. S7†) appeared during the 20 hour reaction (4 cycles), indicating the good photocatalytic stability of the as-fabricated Cd@Al$_2$@Zn.
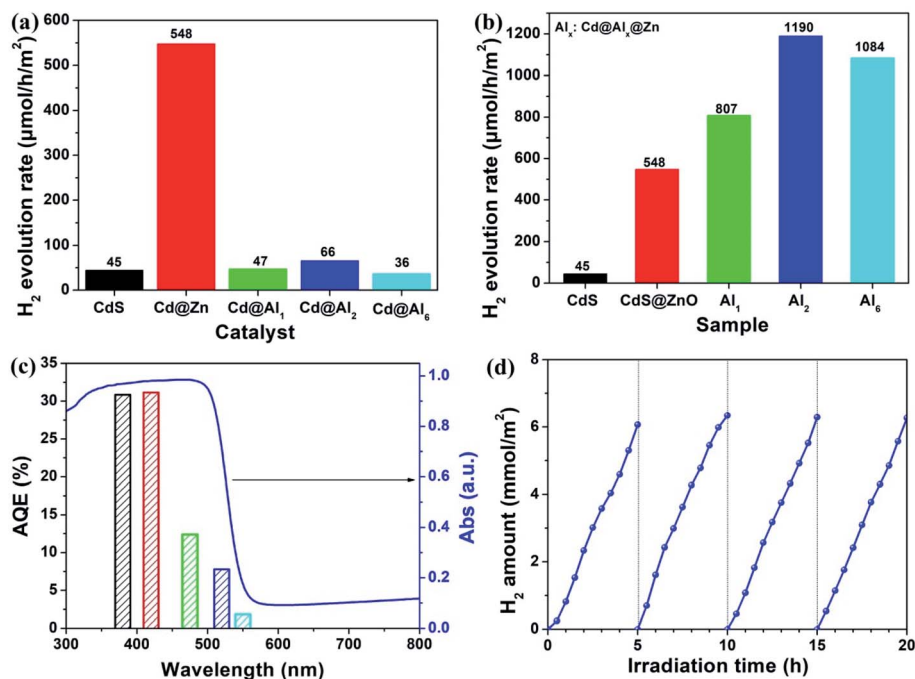

Fig. 2 (a and b) The comparison of photocatalytic H_2 generation rates over the as-fabricated samples based on normalized light absorption ability and specific surface area, the amount of catalysts is 10 mg. (c) The measured AQE of Cd@Al$_2$@Zn at different wavelengths. (d) Long-term cycling reaction test of Cd@Al$_2$@Zn for 20 hours.

Considering that cocatalysts play an important role in the photocatalytic reaction, we further investigated the effect of the Pt cocatalyst by monitoring the H_2 evolution over the Pt-free samples. The H_2 evolution ability of CdS, Cd@Zn and Zd@Al$_2$@Zn in the absence of the Pt cocatalyst is shown in Fig. S8,† and it can be observed that the H_2 evolution rate over Cd@Al$_2$@Zn is much higher than that of Cd@Zn, which is in accord with the performance in the presence of the cocatalyst, indicating that the introduction of the Al$_2$O$_3$ interlayer contributes to the H_2 evolution. In the absence of the Pt cocatalyst, the highest H_2 evolution rate over Cd@Al$_2$@Zn was 201.3 μmol h^{-1}, which is much lower than that in the presence of the Pt cocatalyst (1013.4 μmol h^{-1}), demonstrating that the existence of the Pt cocatalyst is important in facilitating the generation of H_2.

3.2 The role of the ultrathin Al$_2$O$_3$ interlayer

The ultrathin Al$_2$O$_3$ interlayer between CdS and ZnO significantly boosted the photocatalytic hydrogen production. In order to get better understanding of the structure–property relationship in Cd@Al@Zn, we carried out a series of experimental and theoretical studies to disclose the role of the ultrathin Al$_2$O$_3$ interlayer. Fig. S9a† displays the XPS spectra of Cd@Zn and Cd@Al$_2$@Zn, which confirmed the presence of Cd, S, O, and Zn elements, while the signal of Al was detected in Cd@Al$_2$@Zn. The peak of C 1s centered at about 284.5 eV (Fig. S9b†) came from the unavoidably introduced C-based impurity in the carbon tape.[59–61] It should be noticed that the XPS peaks of Cd 3d in Cd@Al$_2$@Zn slightly shifted to lower electronic energies than those in Cd@Zn (Fig. S9c†), but the Zn signal in the two samples was detected at the same position (Fig. S9d†). Since Al$_2$O$_3$ was directly covered on CdS, the lower-shift of the Cd signal in Cd@Al$_2$@Zn can be attributed to the effect of Al$_2$O$_3$ on the chemical environment of CdS, demonstrating the interaction between deposited Al$_2$O$_3$ and the CdS core.[61–63] A weak signal at about 74.1 eV was detected in the Al 2p XPS of Cd@Al$_2$@Zn (Fig. S9e†), which corresponds to the vibration of the Al–O bond,[64–66] confirming the presence of Al$_2$O$_3$. At the same time, the deposition data of ZnO in Cd@Zn and Cd@Al$_2$@Zn determined by XPS are shown in Table S1.† It can be observed that the percentage of Zn increased from 10.11%

for Cd@Zn to 19.90% for Cd@Al$_2$@Zn, demonstrating that the existence of Al$_2$O$_3$ contributes to the adhesion of the ZnO layer, which is in accord with the results of XRD, TEM and SEM measurements.

3.2.1 The passivation effect. Fig. 3a shows the photoluminescence (PL) spectra of pristine CdS, Al$_2$O$_3$ and Cd@Al$_2$ samples. The pristine CdS exhibited a wide region band gap emission with the center at 550 nm wavelength under the excitation of a 370 nm Xe lamp. By contrast, the pure Al$_2$O$_3$ displayed barely an emission signal in the detected region, which may be because the Al$_2$O$_3$ fabricated by the ALD method only responds weakly to ultraviolet light with a wavelength shorter than 350 nm (Fig. S10†). When 2 cycles of Al$_2$O$_3$ was deposited on the surface of CdS, the obtained Cd@Al$_2$ depicted a similar PL spectrum to that of CdS but with much higher emission intensity. Considering that the pure Al$_2$O$_3$ barely has emission in this region, the enhanced PL intensity can be attributed to the suppressed non-radiative relaxation of CdS.[67–69] The photocurrent response of the samples is shown in Fig. S11.† Compared with pure CdS, the Cd@Al$_2$ exhibited an observable enhancement in photocurrent density even with only 2 cycles of Al$_2$O$_3$ deposition. The PL spectra and photocurrent response curves provide direct evidence for the surface passivation effect of the Al$_2$O$_3$ layer. The unavoidable surface defects, dangling bonds and the adsorbates on the surface of CdS NPs inhibit the transfer of charge carriers and consume the excited energy through a non-radiative recombination process, thus quenching the band gap emission of the semiconductor materials.[58,70,71] The introduced Al$_2$O$_3$ layer covers the surface of CdS, repairs the surface defects of CdS and suppresses the formation of dangling bonds and adsorbates, which result in an enhanced band gap emission.[71,72] In addition, Cd@Al$_2$ exhibited a longer PL decay than pure CdS (Fig. 3b), which can be ascribed to the field passivation effect of Al$_2$O$_3$. It was proven that the insulating amorphous Al$_2$O$_3$ has a high fixed negative charge density (10^{12} to 10^{13} cm^{-2}) due to the existence of intrinsic (O interstitials and Al vacancies) and extrinsic (interstitial H) defects,[49,60,73,74] which can consume the photogenerated holes and thus efficiently inhibit the recombination of holes and electrons, prolonging the lifetime of electrons.[72–76]
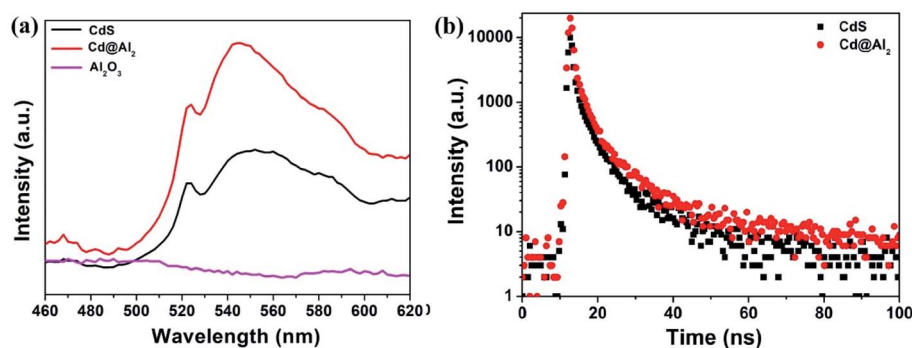

Fig. 3 (a) Photoluminescence spectra of CdS, Al$_2$O$_3$ and Cd@Al$_2$ under the excitation of a 370 nm Xe lamp, normalized by using the UV-vis absorption ability. (b) Time-resolved photoluminescence spectra at 550 nm of CdS and Cd@Al$_2$ catalysts.

11036 | J. Mater. Chem. A, 2020, 8, 11031–11042

This journal is © The Royal Society of Chemistry 2020

The behavior of charge carriers was further investigated to get insight into the passivation effect of the Al_2O_3 layer.[72,77] Fig. 4 shows the Nyquist plots of Cd@Zn and Cd@Al₂@Zn under different measurement circumstances, where a smaller radius reflects relatively low transfer resistance of charge carriers.[75] The EIS curves measured in a dark environment (without light irradiation) give the migration resistance of charge carriers at the electrode interface while those measured under light irradiation relate to the transfer resistance of photogenerated charge carriers.[65,78] In addition, the EIS circles in the lower frequency region show the charge recombination resistance while those in the higher frequency region are related to the charge transfer resistance.[76–80] Cd@Al₂@Zn exhibited the highest charge transfer ability in the dark environment (Fig. 4a) due to the smallest Nyquist radius. Under light irradiation, the EIS curves of Cd@Zn and Cd@Al₂@Zn were recorded under different bias voltages to investigate the electrode polarized action of the measuring system. As can be observed in Fig. S12,† the radius of Nyquist semicircles decreased with the voltage increasing from 0 V to 1.2 V, indicating a continual polarization process of the samples.[77,81] We investigated the Nyquist curves of the samples under 0 V and 0.8 V bias voltages. As shown in Fig. 4b, when the EIS was performed under a bias voltage of 0 V, there was co-existence of recombination and transfer resistance in the catalyst. Cd@Al₂@Zn exhibited a larger Nyquist radius in the low frequency region, indicating that an increased interface charge recombination resistance was caused by the Al_2O_3 interlayer. When the EIS was carried out under a bias of 0.8 V, the built-in electric field and recombination were balanced out under the drive force of the polarization effect. EIS curves give the information about charge transfer resistance. It can be observed from Fig. 4c that the Nyquist radius of Cd@Al₂@Zn was smaller than that of Cd@Zn, indicating that the Al_2O_3 interlayer is beneficial for the decrease of charge transfer resistance. Based on the analysis, it can be concluded from the EIS results that the introduced ultrathin Al_2O_3 interlayer helps to suppress interfacial charge recombination and facilitate the separation of electron–hole pairs, which is very much desired for an efficient photocatalytic reaction.

In order to verify the effect of Al_2O_3 on the capture of photogenerated holes, we further carried out the H_2 evolution reaction in the absence of an extra sacrificial agent, and the results are shown in Fig. S13.† It can be observed that the pure CdS showed barely photocatalytic activity in the absence of a sacrificial agent due to the serious charge carrier recombination. The Cd@Al₂ displayed a H_2 evolution rate of 3.09 μmol h^{-1}, and the improved H_2 evolution rate indicates that the Al_2O_3 ultrathin layer suppresses the recombination of photogenerated charge carriers in CdS. Assuming that the photogenerated holes can't be consumed by Al_2O_3, Cd@Al₂@Zn would display a slightly enhanced H_2 evolution rate in comparison with Cd@Zn due to the improved interface contact. But in fact, much higher H_2 evolution ability was observed over Cd@Al₂@Zn. The dramatically enhanced H_2 evolution rate indicates that the Al_2O_3 consumes the photogenerated holes and plays the role of a sacrificial agent. Fig. S13b† shows the comparison of the H_2 evolution ability of the catalysts with and without an additional sacrificial agent. We noticed that the photocatalytic activity of the Cd@Al@Zn catalyst in aqueous solution was much lower than that with the addition of an external sacrificial agent even though Al_2O_3 plays the role of a sacrificial agent. This is because the addition of Na_2S and Na_2SO_3 not only provides hole acceptors but also results in an alkaline environment with a high pH value for the photocatalytic reaction, which contributes to the splitting of water.[82–84]

Based on the above results and discussion, the surface passivation effect of Al_2O_3 can be understood to be both chemical passivation and field passivation, as follows: (1) amorphous Al_2O_3 synthesized by the ALD strategy has good compatibility and covering capacity on the substrate materials, which help to repair the surface defects and stop the formation of harmful dangling bonds, thus efficiently improving the quality of substrate materials and inhibiting the charge recombination induced by defects through the chemical passivation effect;[50,59,80] (2) due to the existence of fixed negative charges,[73,74] amorphous Al_2O_3 works as a hole trapper, and can effectively consume the photogenerated holes in semiconductors, thus suppressing the recombination of charge carriers by the means of a built-in electric field passivation effect.[58–60,73,74]

In order to clarify the contribution of the introduced Al_2O_3 passivation layer to the improvement of H_2 evolution ability, we
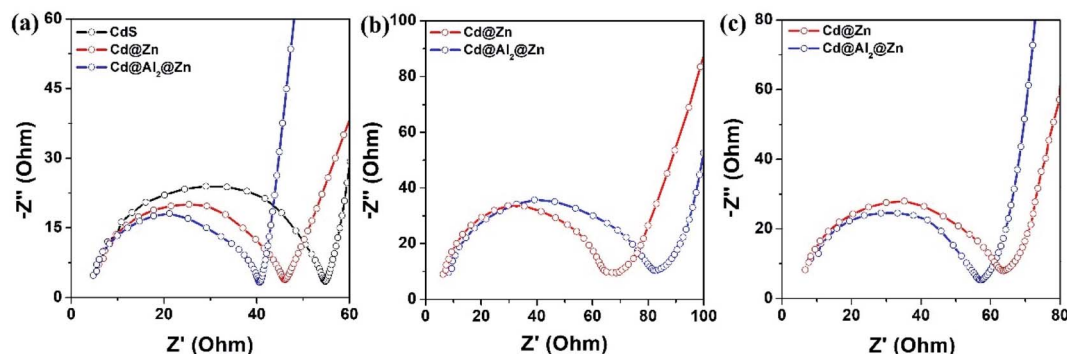

Fig. 4 EIS curves of the catalysts measured at different circumstances: (a) at 0 V bias voltage in the dark; (b and c) at 0 V and 0.8 V bias voltage under 300 W Xe lamp irradiation, respectively.

This journal is © The Royal Society of Chemistry 2020

J. Mater. Chem. A, 2020, **8**, 11031–11042 | **11037**

carefully studied past reports about the interface-passivated design and the performance enhancement of these systems, and the results are listed in Table S3.† Due to the special ability to shrink the interface defects and improve the performance of semiconductor based materials, the strategy of passivation layer has been widely utilized in various fields including photoelectrocatalytic water splitting, CO_2 reduction, solar cells, LED devices and so on in the past ten years. However, barely photocatalytic H_2 evolution has been reported. As was observed, all of the reported systems displayed improved performance, and the strengthening of interface contact and decreased interface defects contribute the most to the enhancement. In our work, the Cd@Al@Zn system exhibited 2.2 times higher H_2 evolution rate than Cd@Zn, and the enhancement coefficient is similar to that in the case of utilization of a passivation layer in other systems. The result demonstrates that we have carried out the first successful attempt to improve the photocatalytic H_2 evolution ability through passivating the interlayer of two semiconductors, which is meaningful in the exploration of high activity photocatalysts.

3.2.2 The tunneling effect. The study on the thickness of the Al_2O_3 interlayer is to reveal the inner charge transfer mechanism in Cd@Al@Zn. Fig. S14a and b† show the EIS and photocurrent response curves of the samples, respectively. In comparison to Cd@Zn, Cd@Al$_1$@Zn and Cd@Al$_2$@Zn displayed obviously decreased charge transfer resistance and increased photocurrent response ability, implying that the charge carriers can transfer through the Al_2O_3 interlayer *via* the tunneling effect when the Al_2O_3 layer is thin enough.[60,71] When the number of deposition cycles of Al_2O_3 was increased to 6, increased transfer resistance and decreased photocurrent response were observed in Cd@Al$_6$@Zn, suggesting that the tunneling effect is decreased due the excessive thickness of the Al_2O_3 layer. According to the equation[63,79] $k_{ET} = k_{ET}^0 \times e^{-\beta d}$ (where k_{ET}, β and d are, respectively, the electron transfer rate, tunneling parameter, and the thickness of the Al_2O_3 layer), when a thicker Al_2O_3 interlayer is introduced, the carrier transfer through the tunneling effect will decline exponentially. Therefore, the over-deposition of the Al_2O_3 interlayer is harmful to the efficient migration of photogenerated electrons.

Mott–Schottky (M–S) plots were collected to ascertain the band edge potentials of the samples. As shown in Fig. S15,† the observed positive slope confirmed the n-type characteristic of the samples.[14,18] It can be determined from the M–S curves that the CB of Cd@Al$_2$ shifted to a more negative region compared to that of pure CdS, which can be ascribed to the field passivation effect caused by Al_2O_3. Under irradiation, the photogenerated holes on the VB of CdS were transferred to the Al_2O_3 layer because of the presence of the negative fixed charges on the surface of amorphous Al_2O_3, while the photogenerated electrons quickly accumulated on the CB of CdS, thus resulting in an upward band bending.[50,66]

The energy band structures of CdS, Al_2O_3 and ZnO were further determined by DFT calculations to clarify the transfer behavior of charge carriers in the Cd@Al@Zn system. The Al_2O_3 displayed a deep valence band (VB) position and a high conductive band (CB) position compared to both CdS and ZnO

(Fig. 5a), indicating its insulating nature. Due to the existence of negative fixed charges,[57,63,65] the holes on the VB of ZnO and CdS can be consumed by Al_2O_3, thus inhibiting the formation of the Z-scheme energy transfer mechanism. The work function of CdS is lower than that of ZnO, and thus the electrons on the CB of CdS will cross over Al_2O_3 through the tunneling effect and finally jump to the CB of ZnO.[59,64,66] The transfer speed of electrons can be determined from the contact potential difference (CPD), which reflects the driving force of charge transfer at the interface between two semiconductors, and a higher CPD means a faster electron transfer speed from one material to another.[65,66,85] The CPD in CdS–ZnO (4.19 eV, Fig. 5b) is much lower than that in CdS–Al_2O_3 (6.69 eV, Fig. 5c) and Al_2O_3–ZnO (7.83 eV, Fig. 5d), implying that the existence of Al_2O_3 helps to trap electrons from CdS and then transfer to the surface of ZnO, realizing the transfer of electrons from the CdS core to the ZnO shell. As a result, the Al_2O_3 interlayer traps the photogenerated electrons from the CdS core and then transfers them to the ZnO shell by the tunneling effect, and meanwhile the photogenerated holes produced in the CdS core and the ZnO shell are efficiently consumed by the negative fixed charges of the Al_2O_3 interlayer, resulting in a modified type II transfer mechanism.

The tunneling effect of the ultrathin Al_2O_3 interlayer was further determined by the detection of active intermediate hydroxyl radicals ($\cdot$OH) over Cd@Zn and Cd@Al$_2$@Zn. Ammonium carbonate (AC), a hole scavenger, was added to the suspension of Cd@Zn (denoted as Cd@Zn + AC for convenience) to distinguish the hole trapping ability of the Al_2O_3 interlayer in Cd@Al$_2$@Zn.[86,87] PL spectra using terephthalic acid (TA) as a probe molecule were measured to detect the formation of $\cdot$OH in the suspension, where a higher PL peak intensity reflects a larger amount of $\cdot$OH. In general, the $\cdot$OH can be generated from both the photogenerated electrons and holes when the CB and VB are in suitable positions.[66,86,87] (1) The photogenerated electrons react with the dissolved oxygen to produce superoxide radical anions ($\cdot O^{2-}$), which further react with hydrogen ions (H^+) to produce $\cdot$OH radicals. (2) The photogenerated holes directly react with hydroxyl ions (OH^-) or water molecules (H_2O) to produce $\cdot$OH radicals. As shown in Fig. 6a, in Cd@Zn (sample I), the electrons on the CB of CdS and the holes on the VB of ZnO contribute to the generation of $\cdot$OH, and a relatively high PL intensity can be observed over Cd@Zn (Fig. 6b). In Cd@Zn + AC (sample II), the holes on the VB of CdS cannot produce $\cdot$OH radicals due to its less positive position than OH^- and H_2O, and the holes on the VB of ZnO can be trapped by AC, so the $\cdot$OH radicals are only generated from the electrons on the CB of CdS and ZnO, resulting in a much lower PL intensity in comparison with Cd@Zn. In Cd@Al$_2$@Zn (sample III), the Al_2O_3 interlayer plays a similar role to AC; the photogenerated holes on the VB of both CdS and ZnO are consumed by its negative fixed charges, which inhibits the generation of $\cdot$OH from the VB of the two semiconductors. Due to the tunneling effect caused by the ultrathin Al_2O_3 interlayer, the photogenerated electrons can be transferred quickly from the CB of CdS to the CB of ZnO, which is adverse to the formation of $\cdot$OH because the electrons on the CB of ZnO have a lower reducing capability than the electrons on the CB of CdS
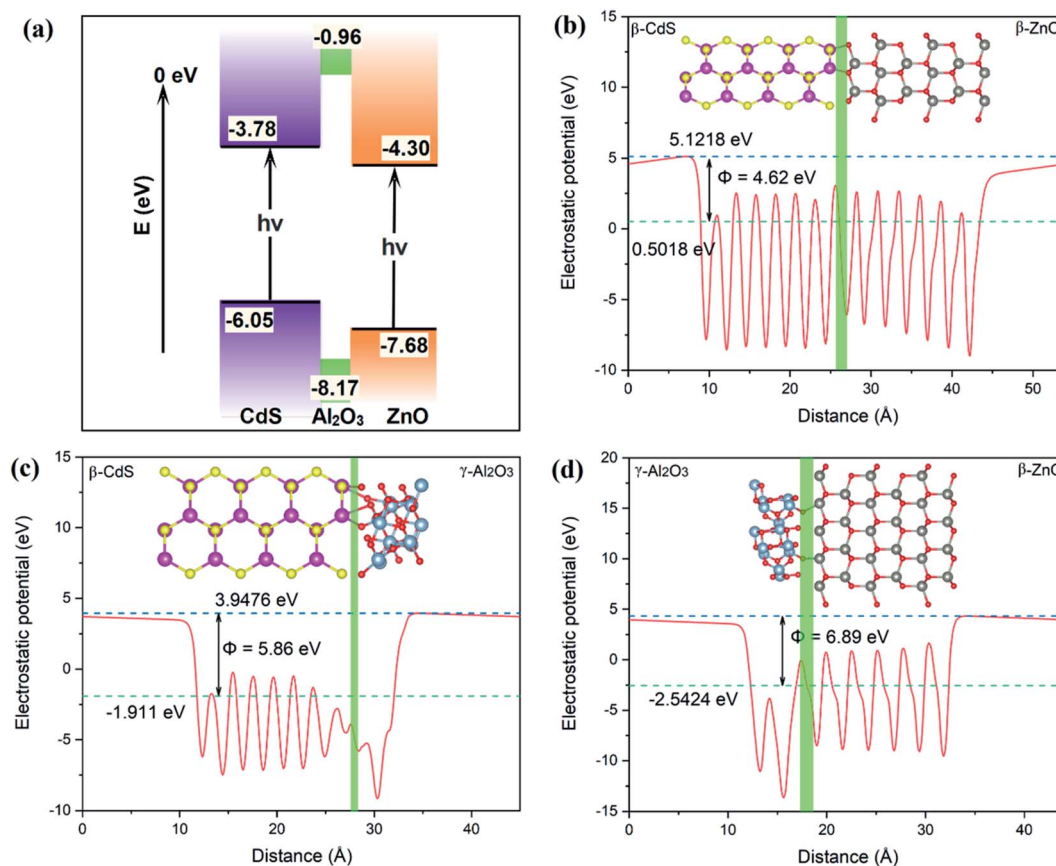
Fig. 5   (a) The calculated energy band position of CdS, Al_2O_3 and ZnO; (b)–(d) the calculated slab module of the energy change along the c-direction of the slab cell for CdS–ZnO, CdS–Al_2O_3 and Al_2O_3–ZnO interfaces, respectively, φ is the calculated contact potential difference.

(the CB position of ZnO is more positive than that of CdS). Therefore, the PL intensity produced from Cd@Al2@Zn will be lower than that from Cd@Zn + AC, as confirmed in Fig. 6b.

3.3   The proposed transfer mechanism of charge carriers

Based on the results and discussion, we can draw a conclusion that the existence of the Al_2O_3 interlayer in Cd@Al@Zn results in a new transfer mechanism of charge carriers, which is totally different from the Z-scheme mechanism in the Cd@Zn system (Scheme 1a). As illustrated in Scheme 1b, after the introduction of Al_2O_3, the holes on the VB of both CdS and ZnO are consumed

by the negative fixed charges of Al_2O_3, which inhibits the direct Z-scheme mechanism. Due to the different energy band positions of CdS and ZnO, the photogenerated electrons transfer from the CB of CdS (higher energy level) to the CB of ZnO (lower energy level), thus forming a modified type II transfer mechanism, which is also different from the traditional type II mechanism because the photogenerated holes do not transfer from the VB of ZnO to that of CdS. The photogenerated electrons transfer along the direction of CdS–Al_2O_3–ZnO, which efficiently suppresses the recombination of charge carriers. Moreover, the photogenerated electrons transferred from the CdS core to the ZnO shell can be consumed effectively in time by H_2O, thus facilitating the
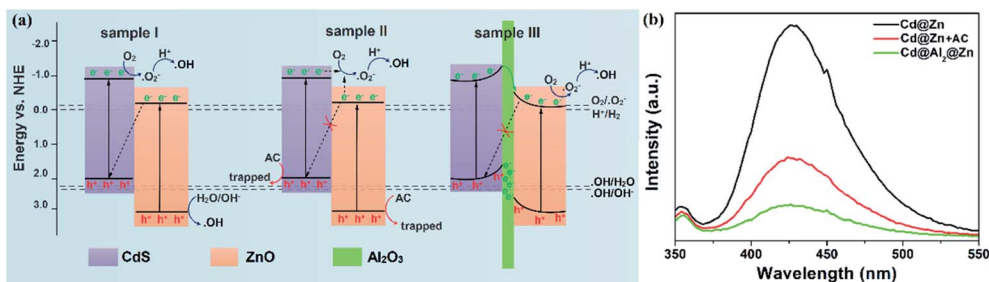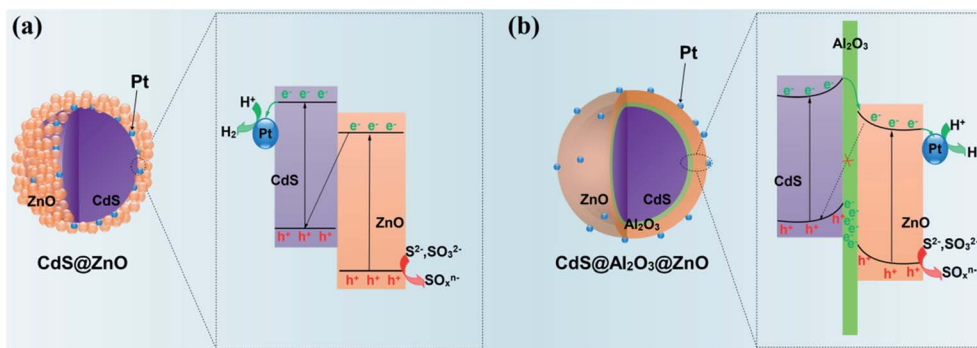

Fig. 6   (a) Pathways of ·OH produced from Cd@Zn (sample I), Cd@Zn + AC (sample II) and Cd@Al2@Zn (sample III); (b) the corresponding PL spectra of the samples.

Scheme 1 The possible energy transfer mechanism in (a) Cd@Zn and (b) Cd@Al@Zn.

generation of H_2. The formation of the modified type-II energy transfer mechanism can also be verified by the discordance between the electron behavior and H_2 evolution ability. It is observed from Fig. S14† that Cd@Al$_6$@Zn presents a smaller photocurrent and a larger electrochemical impedance than Cd@Zn, but the H_2 evolution rate of Cd@Al$_6$@Zn is higher than that of Cd@Zn. The increased H_2 production performance can be ascribed to the exposure of the active reaction surface. In Cd@Zn, a direct Z-scheme energy transfer mechanism is proven, where the photogenerated electrons accumulate on the surface of the CdS core. However, the surface of CdS is partially covered by ZnO nanoparticles, and the contradiction in the exposure of the CdS surface and the formation of a heterojunction between CdS and ZnO is irreconcilable and thus results in a limited H_2 evolution rate. As to Cd@Al@Zn, the photogenerated electrons transferred to the surface of the ZnO shell through the modified type-II mechanism, so the exposure of active reaction sites and the formation of the heterojunction are complementary, thus accelerating the photocatalytic reaction.

4. Conclusions

In summary, an ultrathin Al_2O_3 interlayer was introduced into the interface between the CdS core and the ZnO shell using a facile ALD method. The obtained Cd@Al$_x$@Zn displayed dramatically enhanced photocatalytic hydrogen evolution performance. The optimized Cd@Al$_2$@Zn presented a photocatalytic hydrogen evolution rate of 1190 µmol h^{-1} m^{-2}, which was 2.17 times higher than that of Cd@Zn. The enhanced photocatalytic performance can be attributed to the following reasons: (i) the tunneling effect of the Al_2O_3 interlayer induces the transfer of photogenerated electrons from the CdS core to the ZnO shell, and then the electrons are consumed by H_2O to produce H_2; meanwhile the photogenerated holes are depleted by the fixed negative charges of Al_2O_3, forming a modified type II transfer mechanism. (ii) The surface passivation effect of the ultrathin Al_2O_3 interlayer overcomes the lattice mismatch between wurtzite ZnO and wurtzite CdS, which facilitates the uniform deposition of the ZnO layer and promotes the close contact between interfaces. Benefitting from this, the separation and transfer of charge carriers are efficiently promoted, thus boosting the photocatalytic H_2 generation.

Conflicts of interest

The authors declare no conflict of interest.

References

1 X. Sun, Y. Mi, F. Jiao and X. Xu, *ACS Catal.*, 2018, **8**, 3209–3221.
2 X. Fang, L. Cui, T. Pu, J. Song and X. Zhang, *Appl. Surf. Sci.*, 2018, **457**, 863–869.
3 Y. Zou, J. Shi, D. Ma, Z. Fan, L. Cheng, D. Sun, Z. Wang and C. Niu, *ChemSusChem*, 2018, **11**, 1187–1197.
4 C. Zhao, Z. Wang, X. Li, X. Yi, H. Chu, X. Chen and C. Wang, *Chem. Eng. J.*, 2020, **389**, 123431.
5 J. Chen, X. Zhang, F. Bi, X. Zhang, Y. Yang and Y. Wang, *J. Colloid Interface Sci.*, 2020, **571**, 275–284.
6 F. Qiu, Z. Han, J. J. Peterson, M. Y. Odoi, K. L. Sowers and T. D. Krauss, *Nano Lett.*, 2016, **16**, 5347–5352.
7 X. Yi, S. Ma, X. Du, C. Zhao, H. Fu, P. Wang and C. Wang, *Chem. Eng. J.*, 2019, **375**, 121944.
8 C. Marchal, T. Cottineau, M. G. M. Medrano, C. C. Justin, V. Caps and V. Keller, *Adv. Energy Mater.*, 2018, **8**, 1702142.
9 M. Yang, C. Han and Y. Xu, *J. Phys. Chem. C*, 2015, **119**, 27234–27246.
10 D. Ma, J. Shi, Y. Zou, Z. Fan, J. Shi, L. Cheng and D. Sun, *Nanoscale*, 2018, **10**, 7860–7870.
11 J. Shi, D. Ma, Y. Zou, Z. Fan, J. Shi, L. Cheng, X. Ji and C. Niu, *J. Power Sources*, 2018, **379**, 249–260.

12 Y. Yu, W. Ouyang, Z. Liao, B. Du and W. Zhang, *ACS Appl. Mater. Interfaces*, 2014, **6**, 8467–8474.

13 G. Ai, H. Li, S. Liu, R. Mo and J. Zhong, *Adv. Funct. Mater.*, 2015, **25**, 5706–5713.

14 X. Yang, J. Xu, T. Wong, Q. Yang and C. Lee, *Phys. Chem. Chem. Phys.*, 2013, **15**, 12688–12693.

15 L. Huang, X. Wang, J. Yang, G. Liu, J. Han and C. Li, *J. Phys. Chem. C*, 2013, **117**, 11584–11591.

16 M. Chandra, K. Bhunia and D. Pradhan, *Inorg. Chem.*, 2018, **57**, 4524–4533.

17 A. Torabi and V. N. Staroverov, *J. Phys. Chem. Lett.*, 2015, **6**, 2075–2080.

18 C. Zhao, Z. Wang, X. Li, X. Yi, H. Chu, X. Chen and C. Wang, *Chem. Eng. J.*, 2020, **389**, 123431.

19 M. G. Ahmed, I. E. Kretschmer, T. A. Kandiel, A. Y. Ahmed, F. A. Rashwan and D. W. Bahnemann, *ACS Appl. Mater. Interfaces*, 2015, **7**, 24053–24062.

20 L. Wang, N. T. Nguyen and P. Schmuki, *ChemSusChem*, 2016, **9**, 2048–2053.

21 F. Ye, H. Li, H. Yu, S. Chen and X. Quan, *Appl. Catal., B*, 2018, **227**, 258–265.

22 Y. Xiong, X. Zhu, A. Mei, F. Qin, S. Liu, S. Zhang, Y. Jiang, Y. Zhou and H. Han, *Sol. RRL*, 2018, **2**, 1800002.

23 Y. Zou, J. Shi, D. Ma, Z. Fan, C. Niu and L. Wang, *ChemCatChem*, 2017, **9**, 3752–3761.

24 M. Imran, A. B. Yousaf, P. Kasak, A. Zeb and S. J. Zaidi, *J. Catal.*, 2017, **353**, 81–88.

25 Y. Zou, J. Shi, D. Ma, Z. Fan, L. Lu and C. Niu, *Chem. Eng. J.*, 2017, **322**, 435–444.

26 D. Ma, J. Shi, D. Sun, Y. Zou, L. Cheng, C. He, H. Wang, C. Niu and L. Wang, *Appl. Catal., B*, 2019, **244**, 748–757.

27 D. Ma, J. Shi, Y. Zou, Z. Fan, X. Ji, C. Niu and L. Wang, *Nano Energy*, 2017, **39**, 183–191.

28 S. R. Lingampalli, U. K. Gautam and C. N. R. Rao, *Energy Environ. Sci.*, 2013, **6**, 3589–3594.

29 K. Rajeshwar, A. Thomas and C. Janaky, *J. Phys. Chem. Lett.*, 2015, **6**, 139–147.

30 L. Y. Kunz, L. B. T. Diroll, C. J. Wrasman, A. R. Riscoe and A. M. M. Cargnello, *Energy Environ. Sci.*, 2019, **12**, 1657–1667.

31 G. Dong, M. Fang, H. Wang, S. Yip, H. Cheung, F. Wang, C. Wong, S. Chu and J. C. Ho, *J. Mater. Chem. A*, 2015, **3**, 13080–13086.

32 Z. Shi, K. Nie, Z. Shao, B. Gao, H. Lin, H. Zhang, B. Liu, Y. Wang, Y. Zhang, X. Sun, X. Cao, P. Hu, Q. Gao and Y. Tang, *Energy Environ. Sci.*, 2017, **10**, 1262–1271.

33 G. Kresse and J. Hafner, *Phys. Rev. B: Condens. Matter Mater. Phys.*, 1994, **49**, 14251–14269.

34 G. Kresse and J. Furthmuller, *Phys. Rev. B: Condens. Matter Mater. Phys.*, 1996, **54**, 11169–11186.

35 G. Kresse and J. Furthmuller, *Comput. Mater. Sci.*, 1996, **6**, 15–50.

36 P. Blöchl, *Phys. Rev. B: Condens. Matter Mater. Phys.*, 1994, **50**, 17953–17979.

37 G. Kresse and D. Joubert, *Phys. Rev. B: Condens. Matter Mater. Phys.*, 1999, **59**, 1758–1775.

38 J. Perdew, A. Ruzsinszky, G. Csonka, O. Vydrov, G. Scuseria, L. Constantin, X. Zhou and K. Burke, *Phys. Rev. Lett.*, 2008, **100**(136406), 1–4.

39 J. Heyd, G. Scuseria and M. Ernzerhof, *J. Chem. Phys.*, 2003, **118**, 8207–8215.

40 J. Heyd, G. Scuseria and M. Ernzerhof, *J. Chem. Phys.*, 2006, **124**, 219906.

41 C. Adamo and V. Barone, *J. Chem. Phys.*, 1999, **110**, 6158–6170.

42 J. Paier, R. Hirschl, M. Marsman and G. Kresse, *J. Chem. Phys.*, 2005, **122**(234102), 1–13.

43 L. Shi, Y. Qin, J. Hu, Y. Duan, L. Qu, L. Wu and G. Tang, *Europhys. Lett.*, 2014, **106**(57001), 1–6.

44 V. M. Bermudez, *Surf. Sci.*, 2008, **602**, 1938–1947.

45 S. Dixon, S. Sathasivam, B. Williamson, D. Scanlon, C. Carmalt and I. Parkin, *J. Mater. Chem. C*, 2017, **5**, 7585–7597.

46 H. S. Wei and A. Zunger, *Appl. Phys. Lett.*, 1998, **72**, 2011–2013.

47 H. Zhao, X. Zheng, X. Feng and Y. Li, *J. Phys. Chem. C*, 2018, **122**, 18949–18956.

48 G. Yang, W. Yan, Q. Zhang, S. Shen and S. Ding, *Nanoscale*, 2013, **5**, 12432–12439.

49 F. Peng, Q. Zhou, D. Zhang, C. Lu, Y. Ni, J. Kou, J. Wang and Z. Xu, *Appl. Catal., B*, 2015, **165**, 419–427.

50 B. Hoex, M. C. M. Sanden, J. Schmidt, R. Brendel and W. M. M. Kessels, *Phys. Status Solidi RRL*, 2012, **6**, 4–6.

51 H. K. Sahoo, L. Ottaviano and Y. Zheng, *J. Vac. Sci. Technol., B: Nanotechnol. Microelectron.: Mater., Process., Meas., Phenom.*, 2018, **36**, 011202.

52 J. A. Mann and W. R. Dichtel, *J. Phys. Chem. Lett.*, 2013, **4**(16), 2649–2657.

53 X. Wang, C. Liow, D. Qi, B. Zhu, W. R. Leow, H. Wang, C. Xue, X. Chen and S. Li, *Adv. Mater.*, 2014, **26**, 3506–3512.

54 Q. Cheng, M. K. Benipal, Q. Liu, X. Wang, P. A. Crozier, C. K. Chan and R. J. Nemanich, *ACS Appl. Mater. Interfaces*, 2017, **9**, 16138–16147.

55 X. Zhang, Y. Wang, F. Hou, H. Li, Y. Yang, Y. Yang and Y. Wang, *Appl. Surf. Sci.*, 2017, **391**, 476–483.

56 W. R. Leow, W. K. H. Ng, T. Peng, X. Liu, B. Li, W. Shi, Y. Lum, X. Wang, X. Lang, S. Li, N. Mathews, J. W. Ager, T. C. Sum, H. Hirao and X. Chen, *J. Am. Chem. Soc.*, 2016, **139**, 269–276.

57 R. Wei, P. Kuang, H. Cheng, Y. Chen, J. Long, M. Zhang and Z. Liu, *ACS Sustainable Chem. Eng.*, 2017, **5**, 4249–4257.

58 Z. Liu, J. Zhang and W. Yan, *ACS Sustainable Chem. Eng.*, 2018, **6**, 3565–3574.

59 H. Q. Li, Q. M. Wang, S. M. Jiang, J. Ma, J. Gong and C. Sun, *Corros. Sci.*, 2011, **53**, 1097–1106.

60 Q. Gui, Z. Xu, H. Zhang, C. Cheng, X. Zhu, M. Yin, Y. Song, L. Lu, X. Chen and D. Li, *ACS Appl. Mater. Interfaces*, 2014, **6**, 17053–17058.

61 M. A. Rehman, I. Akhtar, W. Choi, K. Akbar, A. Farooq, S. Hussain, M. A. Shehzad, S. Chun, J. Jung and Y. Seo, *Carbon*, 2018, **132**, 157–164.

62 M. Park, J. Jung, S. Shin, J. Song, Y. Nam, D. Kim and J. Lee, *Thin Solid Films*, 2016, **599**, 54–58.

This journal is © The Royal Society of Chemistry 2020

J. Mater. Chem. A, 2020, **8**, 11031–11042 | 11041

63 F. Ning, M. Shao, S. Xu, Y. Fu, R. Zhang, M. Wei, D. G. Evans and X. Duan, *Energy Environ. Sci.*, 2016, **9**, 2633–2643.

64 W. Li, P. Liu, J. Meng, K. Zhang, F. Ma, X. Liu, X. Chen and D. He, *Surf. Coat. Technol.*, 2016, **286**, 313–318.

65 A. Novikov, *Solid-State Electron.*, 2010, **54**, 8–13.

66 Y. Lin, J. Zhang, E. H. Sargent and E. Kumacheva, *Appl. Phys. Lett.*, 2002, **81**, 3134.

67 S. Liu, F. Liu, H. Guo, Z. Zhang and Z. Wang, *Solid State Commun.*, 2000, **115**, 615–618.

68 S. Deka, A. Quarta, M. G. Lupo, A. Falqui, S. Boninelli, C. Giannini, G. Morello, M. D. Giorgi, G. Lanzani, C. Spinella, R. Cingolani, T. Pellegrino and L. Manna, *J. Am. Chem. Soc.*, 2009, **131**, 2948–2958.

69 S. N. Novikov and S. P. Timoshenkov, *Adv. Colloid Interface Sci.*, 2003, **105**, 329–339.

70 K. Cho and Y. Sung, *Nano Energy*, 2017, **36**, 176–185.

71 F. Le Formal, N. Tétreault, M. Cornuz, T. Moehl, M. Grätzel and K. Sivula, *Chem. Sci.*, 2011, **2**, 737–743.

72 X. Yue, S. Yi, R. Wang, Z. Zhang and S. Qiu, *Appl. Catal., B*, 2018, **224**, 17–26.

73 G. Dingemans, N. M. Terlinden, D. Pierreux, H. B. Profijt, M. C. M. van de Sanden and W. M. M. Kessels, *Electrochem. Solid-State Lett.*, 2011, **14**(1), 1–4.

74 J. Schmidt, B. Veith and R. Brendel, *Phys. Status Solidi RRL*, 2009, **3**(9), 287–289.

75 X. Yi, S. Ma, X. Du, C. Zhao, H. Fu, P. Wang and C. Wang, *Chem. Eng. J.*, 2019, **375**, 121944.

76 J. Fang, J. Gu, Q. Liu, W. Zhang, H. Su and D. Zhang, *ACS Appl. Mater. Interfaces*, 2018, **10**, 19649–19655.

77 W. Ke, C. C. Stoumpos, J. L. Logsdon, M. R. Wasielewski, Y. Yan, G. Fang and M. G. Kanatzidis, *J. Am. Chem. Soc.*, 2016, **138**, 14998–15003.

78 A. G. Scheuermann, J. D. Prange, M. Gunji, C. E. D. Chidseyb and P. C. McIntyre, *Energy Environ. Sci.*, 2013, **6**, 2487–2496.

79 A. C. Nielander, M. J. Bierman, N. Petrone, N. C. Strandwitz, S. Ardo, F. Yang, J. Hone and N. S. Lewis, *J. Am. Chem. Soc.*, 2013, **135**, 17246–17249.

80 J. van der Merwe, K. Uren, G. van Schoor and D. Bessarabov, *Int. J. Hydrogen Energy*, 2014, **39**, 14212–14221.

81 J. Chen, B. Li, J. Zheng, S. Jia, J. Zhao and H. J. Z. Zhu, *J. Phys. Chem. C*, 2011, **115**(14), 7104–7113.

82 M. Antoniadou, S. Sfaelou and P. Lianos, *Chem. Eng. J.*, 2014, **254**, 245–251.

83 Y. Xu, Y. Ye, T. Liu, X. Wang, B. Zhang, M. Wang, H. Han and C. Li, *J. Am. Chem. Soc.*, 2016, **138**, 10726–10729.

84 M. Wang, S. Shen, L. Li, Z. Tang and J. Yang, *J. Mater. Sci.*, 2017, **52**, 5155–5164.

85 K. E. Roelofs, T. P. Brennan, J. C. Dominguez, C. D. Bailie, G. Y. Margulis, E. T. Hoke, M. D. McGehee and S. F. Bent, *J. Phys. Chem. C*, 2013, **117**, 5584–5592.

86 J. Shi, Y. Zou, D. Ma, Z. Fan, L. Cheng, D. Sun, Z. Wang, C. Niu and L. Wang, *Nanoscale*, 2018, **10**, 9292–9303.

87 J. Zhang, L. Li, Z. Xiao, D. Liu, S. Wang, J. Zhang, Y. Hao and W. Zhang, *ACS Sustainable Chem. Eng.*, 2016, **4**, 2037–2046.

11042 | *J. Mater. Chem. A*, 2020, **8**, 11031–11042

This journal is © The Royal Society of Chemistry 2020